Spin Reorientation Associated with a Structural Transition in the Iron Oxycarbonate $Sr_4Fe_2O_6CO_3$

Y. Bréard, C. Michel, M. Hervieu, N. Nguyen,* A. Ducouret, V. Hardy, A. Maignan, and B. Raveau

Laboratoire CRISMAT, ENSICAEN, UMR-CNRS 6508, 6, Boulevard du Maréchal Juin, F14050 Caen Cédex, France

F. Bourée and G. André

LLB, CEA Saclay, 91191 Gif sur Yvette, France

Received January 6, 2004. Revised Manuscript Received April 8, 2004

The oxycarbonate $Sr_4Fe_2O_6CO_3$ has been revisited, using a new synthesis route. Its microstructure has been established by electron microscopy and evidences an orthorhombic−monoclinic distortion at 220 K. The latter is associated with a spin reorientation (≈7°) visible in magnetic susceptibility, heat capacity, and neutron diffraction studies. To understand the structural transition, particular attention has been paid for the carbonate groups: they adopt a specific orientation within a layer but different in successive layers, which involve disorder along $\vec{c}$ and order in the (*a*,*b*) plane and are at the origin of the unusual broadening of the Mössbauer lines.

Introduction

Iron is an attractive candidate for the creation of new oxides owing to its facility to exist in different coordination polyhedra (tetrahedron, pyramid, octahedron, etc.) and to exhibit several stable oxidation states, especially Fe(III) and Fe (IV), which may induce novel magnetic and transport properties. The recent discovery of negative magnetoresistance in the perovskite $SrFeO_{3-\delta}$[1] is a good example, which has considerably renewed the interest in the Sr−Fe−O system. The possibility to build layered structures, the so-called $Sr_{n+1}Fe_nO_{3n+1}$ Ruddlesden−Popper phases,[2] based on the intergrowth of multiple perovskite layers with single rock salt layers, is of interest because of the potential of these materials for new 2D interesting physics. To our knowledge, only the two first members have been isolated in this system, namely, Sr_2FeO_4 (n =1)[3] and $Sr_3Fe_2O_7$ (n = 2).[4] Brisi and Rolando[5] have reported the existence of the n = three-member $Sr_4Fe_3O_{10}$, but unfortunately no single phase can be isolated, whatever the synthesis process used, due to the preferential formation of the perovskite $SrFeO_{3-x}$[6] and of "$Sr_3Fe_2O_7$".[7] However, it has been shown that a single phase could be obtained with approximately the same lattice parameters, by totally or partially[7,8] replacing the FeO_6 octahedra of the middle perovskite layer by carbonate groups. These oxycarbonates are not strictly speaking RP phases, but the two structural types exhibit very close relationships. All the works devoted to these iron oxides and oxycarbonates report their high sensitivity to the synthesis process conditions (temperature, atmosphere, pressure, moisture, etc.).

This paper deals with an accurate and fine structural and magnetic study of one $Sr_4Fe_2O_6CO_3$ sample, synthesized under a moisture-free and controlled atmosphere. The magnetic properties evidence a magnetic transition due to a spin reorientation, coupled with a structural transition. The two transitions are characterized using Mössbauer, electronic diffraction, HREM, magnetic susceptibility, and heat capacity.

Experimental Section

Synthesis. The polycrystalline single-phase sample was obtained with a two steps method: first, a precursor was synthesized from an appropriate mixture of SrO, $SrCO_3$, and Fe_2O_3. SrO, freshly prepared by heating SrO_2 up to 1100 °C for 24 h, was introduced still burning in a glovebox under an inert atmosphere to avoid carbonation or moisture. It was last weighed and intimately mixed with the other precursors (dry $SrCO_3$ and Fe_2O_3). The intimately ground powders were then pressed in the form of bars and introduced into silica tubes. All the parts of this handling were carried out in a drybox. The tubes were then sealed under vacuum and heated to 1200 °C for 12 h. Heating and cooling to room temperature were performed in 6 h. In a second step, the precursor was subjected to annealing (heating to 500 °C for 30 min and quenched) under air, leading to the $Sr_4Fe_2O_6CO_3$ compound. About 7 g of $Sr_4Fe_2O_6CO_3$ were prepared by batches of about 1 g, according to this procedure.

* To whom correspondence should be adressed. E-mail: ninh.nguyen@ensicaen.fr.

(1) Maignan, A.; Martin, C.; Nguyen, N.; Raveau, B. *Solid State Sci.* **2001**, *3*, 57.
(2) Ruddlesden, S. R.; Popper, P. *Acta Crystallogr.* **1957**, *10*, 538; **1958**, *11*, 54.
(3) Dann, S. E.; Weller, M. T.; Currie, D. B. *J. Solid State Chem.* **1991**, *92*, 237.
(4) Dann, S. E.; Weller, M. T.; Currie, D. B. *J. Solid State Chem.* **1992**, *97*, 179.
(5) Brisi, C.; Rolando, P. *Ann. Chim. (Rome)* **1969**, *59*, 385.
(6) Bréard, Y. Ph. D. Thesis, Caen University, Dec 2002; p 58.
(7) Yamaura, K.; Huang, Q.; Lynn, J. W.; Erwin, R. W.; Cava, R. J. *J. Solid State Chem.* **2000**, *152*, 374.
(8) Bréard, Y.; Michel, C.; Hervieu, M.; Raveau, B. *J. Mater. Chem.* **2000**, *10*, 1043.

10.1021/cm0401241 CCC: $27.50
Published on Web 06/23/2004

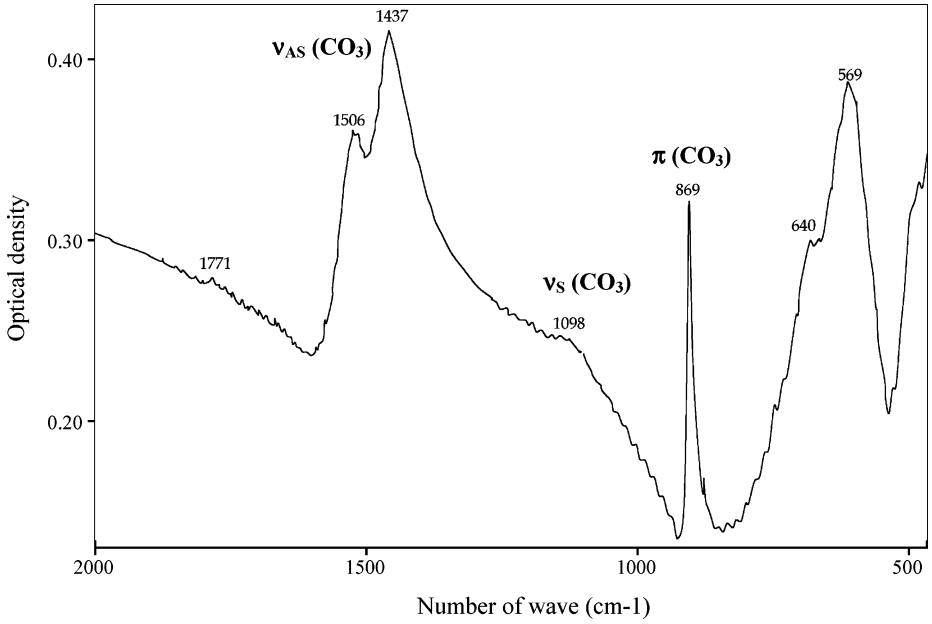

Figure 1. Infrared spectrum of $Sr_4Fe_2O_6CO_3$ registered at room temperature.

Structural Analysis. The samples for electron microscopy were prepared by crushing the crystals in butanol. The flakes in suspension were deposited onto a holey carbon film, supported by a copper grid. The electron diffraction (ED) investigation was carried out with a 2010 JEOL electron microscope. The reciprocal space was characterized by tilting around the crystallographic axes vs temperature between 92 K and RT. The high-resolution electron microscopy (HREM) study was performed with a TOPCON 002B, operating at 200 kV and having a point resolution of 1.8 Å. The interpretation of the HREM images was carried out on the basis of the theoretical images calculated by varying the focus and crystal thickness values, with a Mac Tempas Program. The two microscopes are equipped with an energy dispersive spectroscopy (EDS) analyzer.

The presence of CO_3 groups was checked by infrared spectroscopy measurement. Data have been collected in transmission mode, in the range 450−2000 cm^{-1}, on a commercial instrument, Nicolet 500 using Fourier transforms.

Phase purity was checked by X-ray diffraction using a Philips vertical diffractometer PW1830 equipped with a graphite secondary monochromator and working with Cu Kα radiation. Data were collected by step scanning of 0.025° (2θ) over an angular range $5° < 2\theta < 120°$.

Neutron powder diffraction data were collected at LLB (Saclay-France) on two different diffractometers. One was the high-resolution 3T2 diffractometer where data were collected at three temperatures: 500, 300 and 5 K, using the wavelength 1.2251 Å, in the angular range $6° < 2\theta < 126°$ with steps of 0.05° (2θ), to determine the nuclear cell. The second diffractometer was the G41 and data were collected at several temperature in the range 1.5−290 K, using the wavelength 2.4266 Å, in the angular range $1.5° < 2\theta < 80°$, to determine the magnetic cell. The scattering lengths of the differents atoms were those included in the Rietveld profile analysis program package (FULLPROF[9]).

Physical Characterizations and Mössbauer Spectroscopy. The physical properties were measured with a Physical Properties Measurements System (four-probe resistivity and heat capacity) and an ac−dc Squid magnetometer (magnetic susceptibility, magnetization field dependence), both systems from Quantum Design Compagny. The dielectric characteristics were acquired at 1 MHz-1 V with a FLUCKE 6306 LCR meter.

The ^{57}Fe Mössbauer spectra of the powdered sample collected at different temperatures in the range 80−500 K were recorded in transmission mode, using a conventional spectrometer operating in the constant acceleration mode. ^{57}Co/Rh was used as the γ-ray source. The spectra were fitted with a Lorentzian line shape using the computer program MOSFIT;[10] the isomer shift (IS) is referred to metallic iron.

Results and Discussion

(1) Preliminary Characterization (Room Temperature). Sample was characterized by X-ray diffraction to check the phase purity and to determine the cell parameters. Apart from some weak diffraction peaks characteristic of unreacted $SrCO_3$ at low levels which are observed, all the diffraction lines can be indexed in a tetragonal cell with parameters $a_T = 3.88965(3)$ Å and $c_T = 27.9906(1)$ Å, SG: $I4/mmm$.

The presence of CO_3 groups was confirmed by infrared spectroscopy. On the spectrum shown in Figure 1, the peak occurring at 869 cm^{-1} corresponds to the characteristic π (CO_3) bonding, indicating that CO_3 groups are actually present in the heart of the crystallites. The splitting of the line corresponding to the ν antisymmetric bonding, ν_{as} (1437 and 1506 cm^{-1}), and the shape of the line corresponding to the ν symmetric bonding, ν_s (1096 cm^{-1}), indicate that the CO_3 groups adopt two kinds of configurations with one more "free" (from the point of view of C−O bonds) than the other. This information agrees with the structural results (see after).

The EDS analysis performed on numerous microcrystallites shows a great homogeneity of the samples and confirms the cationic composition Sr/Fe = 2. The iron oxidation state was determined by XANES and Mössbauer spectroscopy at room temperature. All techniques agree with trivalent iron. The oxygen content, determined by redox back-titration (RBT) as described elsewhere,[11] is found to be very close to the expected one.

(9) Rodriguez Carvajal, J. Collected Abstract of Satellite Meeting on Powder Diffraction of XVth Crystallographic Union Int. Congr., Toulouse, 1990, p 127.

(10) Varret, F.; Teillet, J. Université du Maine, France, unpublished.

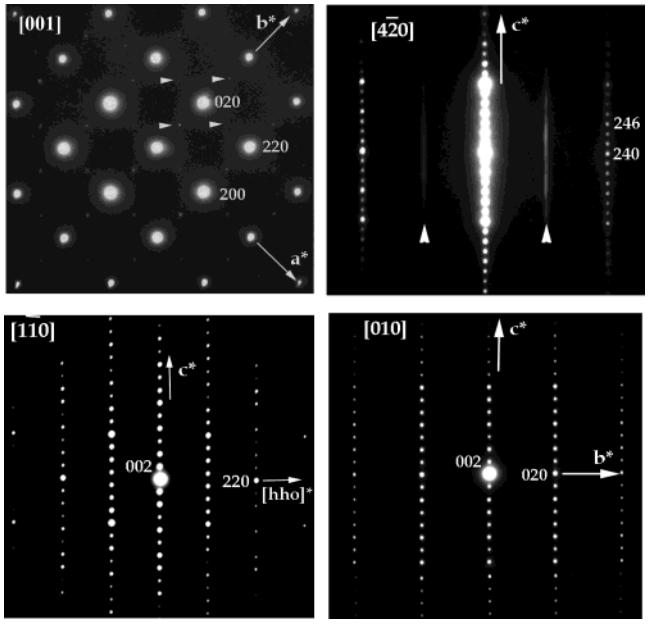

Figure 2. (a) [001], (b) [4$\bar{2}$0], (c) [1$\bar{1}$0], and (d) [010] ED pattern of $Sr_4Fe_2O_6CO_3$ registered at room temperature.

So within the limit of the techniques accuracy, we can assume that our sample has the composition $Sr_4Fe_2O_6CO_3$. Note that, in the course of the neutron diffraction refinements, other different models have been unsuccessfully tested (considering oxygen, iron, and CO_3 and nonstoichoimetry), confirming this result.

(2) Electron Microscopy Study at Room Temperature. Reconstructing the reciprocal space evidences that the intense reflections are consistent with the *I*4/*mmm* space group. However, all the crystallites systematically exhibit a second system of weak reflections. In the [001] ED patterns, they appear as point-like spots at $^1/_2$ $^1/_2$ 0 (white triangles in Figure 2a) and involve a doubling of the cell: $a \approx b \approx a_T\sqrt{2}$. Viewing the crystals perpendicularly to the *c** axis shows that these reflections are elongated, often resulting in diffuse streaky lines, as shown in the [4$\bar{2}$0] ED patterns (indicated by white triangles in Figure 2b) and not visible along [1$\bar{1}$0] and [010] (Figure 2c,d). The reconstruction of the reciprocal space leads to an orthorhombic cell, with $a = b = a_T\sqrt{2}$ and $c = 28$ Å, and the conditions of reflections (hkl: $k + l = 2n$; $hk0$: ($k = 2n$), $0kl$: $k = 2n$ and $l = 2n$, $h0l$: ($h = 2n$ and $l = 2n$)) are consistent with the *Aba*2 space group.

It clearly appears that twinning phenomena, due to the orthorhombic distortion of the cell, and double diffraction are necessary for indexing the [001] pattern. The elongated shape of the extra reflections along the perpendicular direction suggests the existence of microtwinning domains randomly oriented along $\vec{c}$, in successive layers.

HREM study allows one to understand the origin of the extra reflections and disorder phenomena in this compound. The nature and the stacking mode of the different layers are easily visible by viewing the crystals along [1$\bar{1}$0], as shown in Figure 3 recorded for a focus value close to −15 nm; that is, the bright dots are correlated to the light electron density zones. The brighter dots are correlated to the atomic positions of the CO_3 groups, giving a cross-shaped contrast characteristic of the carbonates, as previously observed in the superconducting copper oxycarbonates.[12] These "carbonate" rows are 14 Å spaced along $\vec{c}$ and 3.8 Å shifted along [110], in agreement with the cell symmetry. The two rows of staggered black dots are correlated with the Sr positions of the rock salt-type layers. The HREM study of numerous crystallites shows that the stacking mode of the different layers is highly regular, without any intergrowth defects.

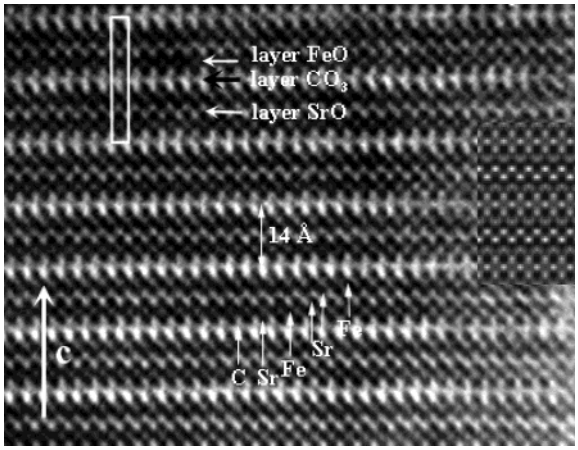

Figure 3. [1$\bar{1}$0] HREM of $Sr_4Fe_2O_6CO_3$. The Sr, Fe, and C atoms positions are indicated by white arrows. The calculated image (crystal thickness: 30 Å, focus value: −150 nm) is superposed on the experimental one.

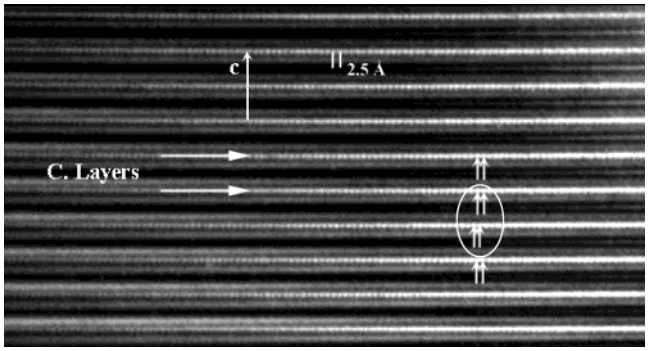

Figure 4. [4$\bar{2}$0] HREM of $Sr_4Fe_2O_6CO_3$, showing that the short-range ordering correlated with the extra reflection in the ED patterns (Figure 2b) arises at the carbonate layers level (white arrows); that one appears as rows of bright dots.

Viewing the crystals along [2$\bar{1}$0] and/or [1$\bar{2}$0] (Figure 4) shows that the superstructure is only visible at the level of the carbonate layers (see white arrows). The contrast consists of alternating bright spots spaced by about 2.5 Å ($2d_{420}$ and/or $2d_{240}$). In the adjacent carbonate rows, this effect is just translated by $\vec{c}$ or suffers an additional shifting by 1.25 Å, involving a local centered contrast (see white arrows) depending on the local orientation of the microtwinning domain. No long-range ordering in the relative arrangement of these bright dots is observed along $\vec{c}$, generating the streaks along $\vec{c}$. This feature is similar to those previously observed in other layered carbonates;[13−15] it is related to the specific

(11) Er-Rakho, L.; Michel, C.; Raveau, B. *J. Solid State Chem.* **1988**, *73*, 514.

(12) Huvé, M.; Michel, C.; Maignan, A.; Hervieu, M.; Martin, C.; Raveau, B. *Physica C* **1993**, *205*, 219.

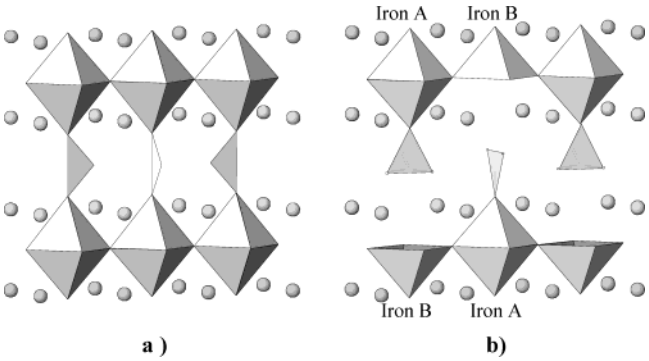

Figure 5. Flag (a) and coat-hanger (b) configuration of the carbonate groups.

orientations of the carbonate groups within the same layer to avoid too short oxygen−oxygen distances between two neighboring CO_3 groups.

In conclusion, the lowering of the symmetry from the tetragonal ideal cell to the actual orthorhombic one and the specific organization of carbonate groups within one layer are clearly evidenced by ED and the HREM characterization. However, it is straightforward that the high degree of "disorder" of the carbonate arrangement along $\vec{c}$ cannot be accounted for with the NPD structure refinement. Consequently, the space group *I*4/*mmm* has been used for this determination of the structure.

(3) Neutron Diffraction Study: Nuclear Structure. The initial structure analysis was made on the 500 K ND data to work with a diffraction pattern free of magnetic contributions (see Mössbauer section). Calculations were carried out in the space group *I*4/*mmm* and all the atoms, except those involved in the triangular carbonate group, were located according to previous structural studies.[7−8,15−19] Three possible configurations of the carbonate groups were considered: (1) the "flag" configuration (F) observed for $Sr_4Sc_2O_6CO_3$[17] and $Sr_2CuO_2CO_3$[18] (see Figure 5a), (2) the "coat hanger" configuration (CH) observed for $Sr_4FeCrO_6CO_3$[16] (see Figure 5b), and (3) the coexistence of both flag and coat hanger configurations with equal amounts used by Yamaura.[7]

These configurations have been tested considering anisotropic thermal displacements for all atoms, except for oxygen belonging to the carbonate groups. The best fit was obtained for the third model with agreement factors: Rp = 3.71%, Rwp = 4.44%, $\chi^2 = 2.55$, and R_B = 4.52%. The difference diffraction pattern drawing in Figure 6 attests to the goodness of the fit. The atomic positions and distances (Tables 1 and 2) are very close to those reported in ref 7 at 400 K. Attempts to modify the ratio F/CH do not improve the fit goodness. Let us recall that the interatomic distances show that the coordination of iron can be described as a compressed tetragonal pyramid (the sixth oxygen neighbor, which belongs to the CO_3 groups, sits much further apart) and that the CO_3 groups are characterized by two short C−O bonds and a long one whatever their configuration "coat hanger" (compare for instance the C−O(3) and C−O(4) distances) or "flag" (compare the C−O(5) and C−O(6) distances). The O−C−O angles range from 115° to 130°

Table 1

A. Structural Parameters of $Sr_4Fe_2O_6CO_3$ at 500 K (First Line) and 300 and 5 K (Second and Third Lines, Respectively) Obtained from NPD Data

atom	site	*x*	*y*	*z*	U_{iso} (Å^2)	*n*
Sr(1)	4e	0	0	0.57249(12)		4
				0.57248(18)		
				0.57206(18)		
Sr(2)	4e	0	0	0.70050(10)		4
				0.70081(15)		
				0.70075(15)		
Fe	4e	0	0	0.14366(8)		4
				0.14334(12)		
				0.14356(12)		
C	2a	0.0	0.0	0.0		2
O(1)	4e	0	0	0.21145(16)		4
				0.21097(21)		
				0.21107(24)		
O(2)	8g	0	0.5	0.13118(8)		8
				0.13105(12)		
				0.13108(15)		
O(3)	4e	0	0.0	0.0501(8)	0.0255(2)[a]	1
				0.0503(9)	0.0180(4)[b]	
				0.0531(12)	0.0155(3)[c]	
O(4)	16n	0.281(5)	0.0	0.0184(6)	0.0255(2)[a]	2
		0.271(6)		*0.0194(9)*	0.0180(4)[b]	
		0.258(6)		0.0224(9)	0.0155(3)[c]	
O(5)	16n	0.144(5)	0.0	0.0393(6)	0.0255(2)[a]	2
		0.138(6)		*0.0390(6)*	0.0180(4)[b]	
		0.093(6)		0.0433(9)	0.0155(3)[c]	
O(6)	8i	0.353(7)	0.0	0.0	0.0255(2)[a]	1
		0.362(9)			0.0180(4)[b]	
		0.349(9)			0.0155(3)[c]	

space group: *I*4/*mmm*

$a = 3.90045(5)$ Å;	$c = 28.0397(6)$ Å
$a = 3.88877(6)$ Å	$c = 27.9820(6)$ Å
$a = 3.87707(6)$ Å	$c = 27.9315(6)$ Å

$\chi^2 = 2.55$	$R_{Bragg} = 4.52\%$	$R_p = 3.71\%$	$R_{wp} = 4.44\%$
$\chi^2 = 3.75$	$R_{Bragg} = 3.91\%$	$R_p = 3.57\%$	$R_{wp} = 4.35\%$
$\chi^2 = 4.94$	$R_{Bragg} = 4.42\%$	$R_p = 4.40\%$	$R_{wp} = 5.30\%$

B. Temperature Factors for $Sr_4Fe_2O_6CO_3$ at 500 K (First Line), 300 K (Second Line), and 5 K (Third Line)

atom	U_{11} (Å^2)	U_{22} (Å^2)	U_{33} (Å^2)	U_{eq} (Å^2)
Sr(1)	0.0116(9)	$=U_{11}$	0.0149(14)	0.0127(10)
	0.0078(7)		0.0124(14)	0.0093(9)
	0.0053(7)		0.0023(12)	0.0043(9)
Sr(2)	0.0094(8)	$=U_{11}$	0.0121(14)	0.0103(10)
	0.0055(6)		0.0107(12)	0.0072(8)
	0.0000(6)		0.0000(9)	0.0000(7)
C	0.0162(14)	$=U_{11}$	0.0199(18)	0.0174(15)
	0.0146(14)		0.0191(15)	0.0161(14)
	0.0119(11)		0.0159(15)	0.0132(12)
Fe	0.0072(8)	$=U_{11}$	0.0086(9)	0.0077(8)
	0.0055(9)		0.0050(8)	0.0053(9)
	0.0009(5)		0.0008(6)	0.0009(5)
O(1)	0.0190(8)	$=U_{11}$	0.0097(14)	0.0159(10)
	0.0128(7)		0.0035(15)	0.0097(10)
	0.0037(7)		0.0014(8)	0.0029(7)
O(2)	0.0116(12)	0.0072(11)	0.0217(15)	0.0135(13)
	0.0080(10)	0.0055(11)	0.0150(12)	0.0095(11)
	0.0041(5)	0.0008(5)	0.0092(4)	0.0047(5)

[a−c] Constrained to have the same value.

(13) Milat, O.; VanTendeloo, G.; Amelinks, S.; Babu, T. G. N.; Greaves, C. *J. Solid State Chem.* **1992**, *97*, 4005.
(14) Miyasaki, Y.; Yamane, H.; Kajitani, T.; Oku, T.; Hiraga, K.; Morii, Y.; Fuchizaki, F.; Funahashi, S.; Hirai, T. *Physica C* **1992**, *191*, 434.
(15) Bréard, Y.; Michel, C.; Hervieu, M.; Nguyen, N.; Studer, F.; Maignan, A.; Raveau, B.; Bourée, F. *J. Solid State Chem.* **2003**, *170*, 424.
(16) Bréard, Y.; Michel, C.; Hervieu, M.; Ducouret, A.; Nguyen, N.; Studer, F.; Maignan, A.; Raveau, B.; Suard, E. *Chem. Mater.* **2001**, *13*, 2423.
(17) Bréard, Y.; Michel, C.; Maignan, A.; Raveau, B. *Chem. Mater.* **2003**, *15*, 1273.
(18) Babu, T. G. N.; Fish, D. J.; Greaves, C. *J. Mater. Chem.* **1991**, *1*, 677.
(19) Robbins, M.; Weryheim, G. K.; Menth, A.; Sherwood, R. C. *J. Phys. Chem. Solids* **1969**, *30*, 1823.

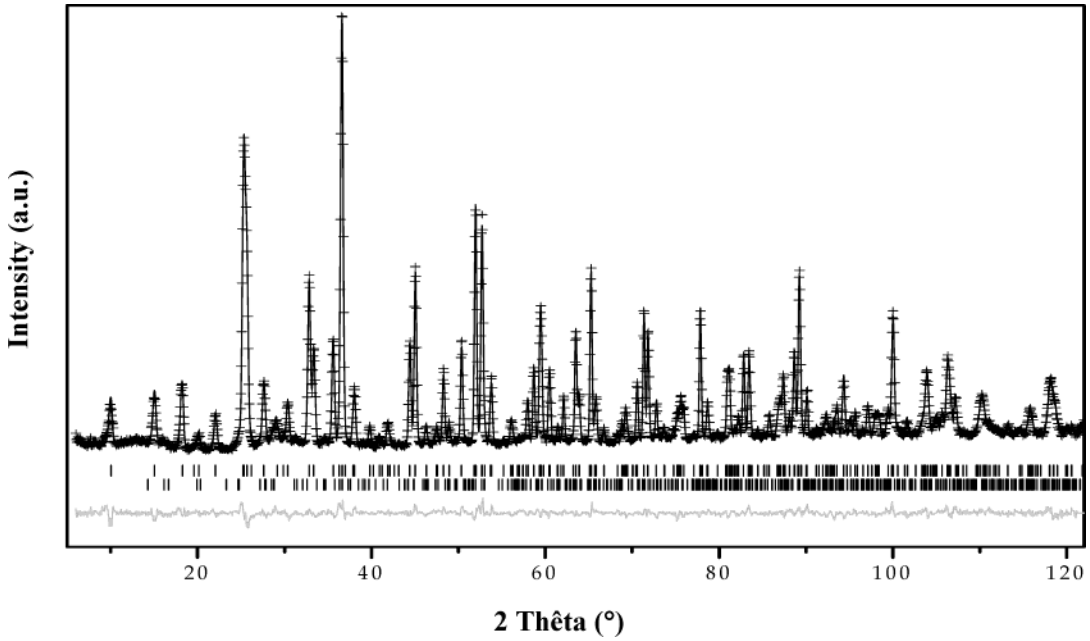

Figure 6. Experimental (crosses), calculated and difference (solid lines) neutron powder diffraction pattern of $Sr_4Fe_2O_6CO_3$ at the end of refinement. The vertical bars are the Bragg angle positions for the main phase (upper) and the impurity $SrCO_3$ (lower).

Table 2. Selected Interatomic Distances and Angles for $Sr_4Fe_2O_6CO_3$ at 500 K (First Line), 300 K (Second Line), and 5 K (Third Line)

M−	O	*d* (Å)	×	*n*[a]	M−	O	*d* (Å)	×	*n*[a]
Sr(1)−	O(2)	2.542(4)	×	4	Fe−	O(1)	1.901(9)	×	1
		2.542(3)					1.889(9)		
		2.540(3)					1.886(9)		
	O(3)	2.829(3)	×	1		O(2)	1.981(1)	×	4
		2.818(3)					1.975(1)		
		2.792(3)					1.971(1)		
	O(4)	2.614(15)	×	1		O(3)	2.623(18)	×	0.25
		2.602(18)					2.604(16)		
		2.560(18)					2.525(19)		
	O(5)	2.569(15)	×	1		O(5)	2.980(14)	×	0.5
		2.575(15)					2.969(15)		
		2.625(16)					2.824(15)		
	O(6)	2.875(9)	×	1					
		2.859(9)							
		2.855(9)							
					C−	O(3)	1.405(19)	×	0.5
							1.409(16)		
							1.485(18)		
Sr(2)−	O(1)	2.469(6)	×	1		O(4)	1.211(17)	×	1
		2.468(6)					1.187(16)		
		2.463(6)					1.182(17)		
	O(1)	2.775(1)	×	4		O(5)	1.237(17)	×	1
		2.764(1)					1.218(16)		
		2.757(1)					1.262(17)		
	O(2)	2.753(3)	×	4		O(6)	1.377(22)	×	0.5
		2.756(3)					1.411(20)		
		2.752(3)					1.354(22)		

Angles O−C−O (deg)

Triangle O(4)−O(3)−O(4)					Triangle O(5)−O(6)−O(5)				
O(3)−C−O(4)	115.2(4)	×	2		O(5)−C−O(5)	126.0(9)	×	1	
	117.3(4)					127.6(5)			
	122.0(4)					146.7(6)			
O(4)−C−O(4)	129.6(6)	×	1		O(5)−C−O(6)	117.0(4)	×	2	
	125.4(6)					116.1(3)			
	116.0(6)					106.6(4)			

[a] In the distance list, the numbers of neighboring oxygen atoms of the elements (*n*) are calculated, taking into account the oxygen site occupancies.

whatever the configuration. The amount of unreacted $SrCO_3$ was refined to 1.6 wt %.

At 300 and 5 K, the neutron diffraction data do not allow detection of any significant change in the symmetry and structural parameters. What is observed is only an increase of the width of the diffraction peaks at low temperature with regard to room temperature and 500 K. This is attributed to the slight cell distortion observed by electron microscopy which appears at low temperature (see section 5) and which is too weak to be seen by neutron diffraction techniques. Results are listed in Tables 1 and 2: one can see that atomic position displacements (due to the temperature variations) are very weak. Attempts of introducing nonstoichiometry on oxygen, iron, or carbon sites were unsuccessful. An example of a possible structure of $Sr_4Fe_2O_6CO_3$ is given in Figure 7.

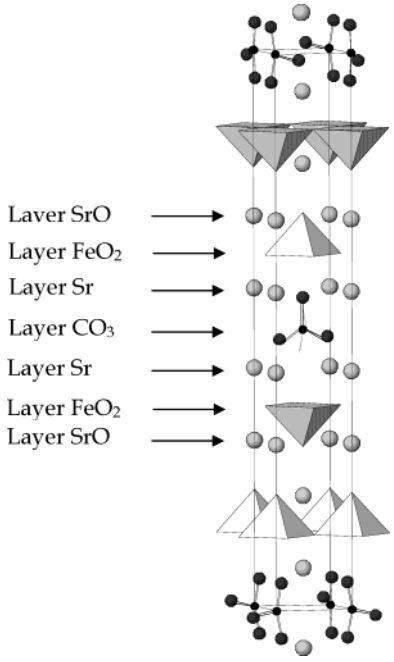

Figure 7. Example of a possible structure of $Sr_4Fe_2O_6CO_3$.

(4) Neutron Diffraction Study: Magnetic Structure. The room-temperature neutron diffraction diagram exhibits extra peaks due to magnetic ordering which can be indexed in a magnetic cell $a_M = b_M =$

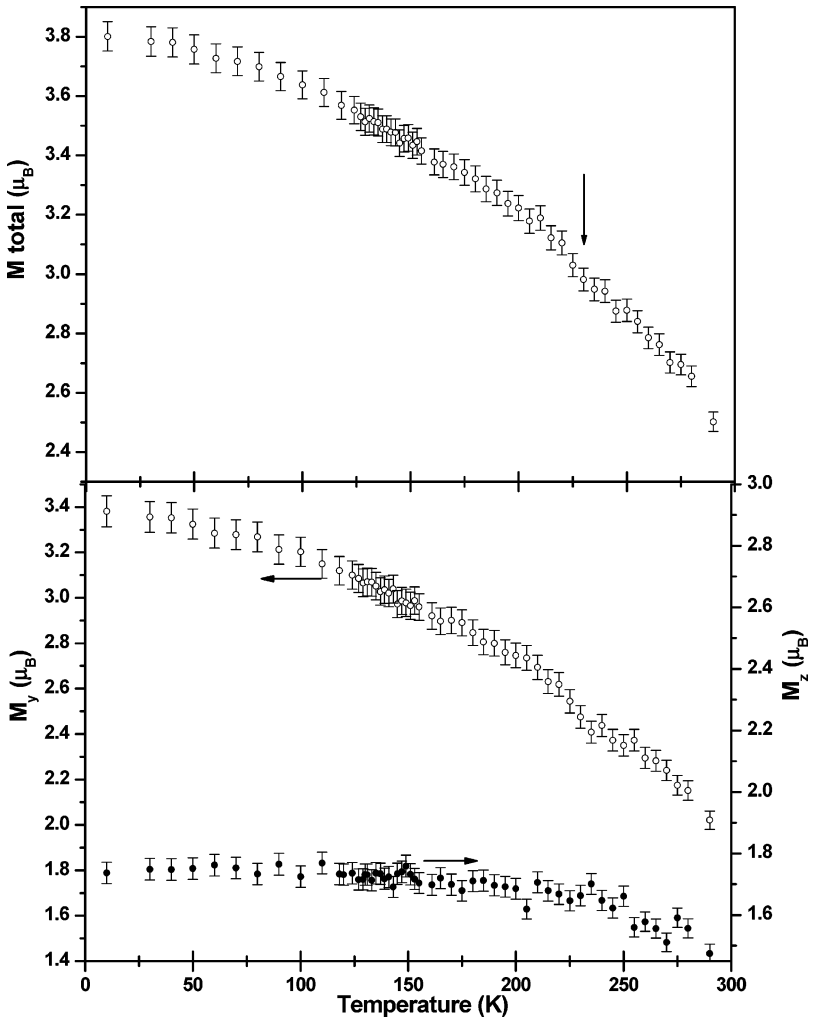

Figure 8. Evolution of the magnetic moment (a) and of the magnetic components (b) as a function of the temperature.

$a_T\sqrt{2}$ and $c_M = c = 28$ Å. The magnetic structure was studied from data collected with the G41 diffractometer in the range 1.5−290 K. Our results confirm those previously established:[7] the iron magnetic moments are in-plane antiferromagnetically coupled and ferromagnetically coupled between planes. At 1.5 K, the iron magnetic moment value is 3.79 μ_B, that is, smaller than the expected value for HS Fe^{3+} (5 μ_B). It lies in the (010) plane of the magnetic cell with two components: Mz = 1.76(5) μ_B and Mx = 3.36(3) μ_B resulting from a tilting of M with respect to the c axis by $\theta = 62°$.

As the temperature increases, M decreases continuously to reach 2.5 μ_B at 290 K as shown in Figure 8. A small event is scarcely visible at about 225 K (black arrow in Figure 8) and could be considered as not significant if the plot of the components of the magnetic moment as a function of temperature did not reveal some interesting features: the variation of Mx looks like that of M, but the event at 220−225 K is more visible; more interestingly, in this temperature range, Mz becomes temperature independent. That means that the component along the c axis saturates below $T \approx 225$ K involving a gradual rocking of the magnetic moment toward the (a,b) plane of about 7° as the temperature decreases ($\theta_{225K} \approx 55°$).

The variation of the cell parameters versus temperature (Figure 9) shows a continuous increase of a and c with T, in agreement with a thermal expansion. However, the a variation exhibits a small discontinuity at 225 K, which can probably be correlated to the magnetic event. To try to understand what structurally happened at this temperature, which does not influence the nuclear structure, an electron microscopy study was carried out at low temperature.

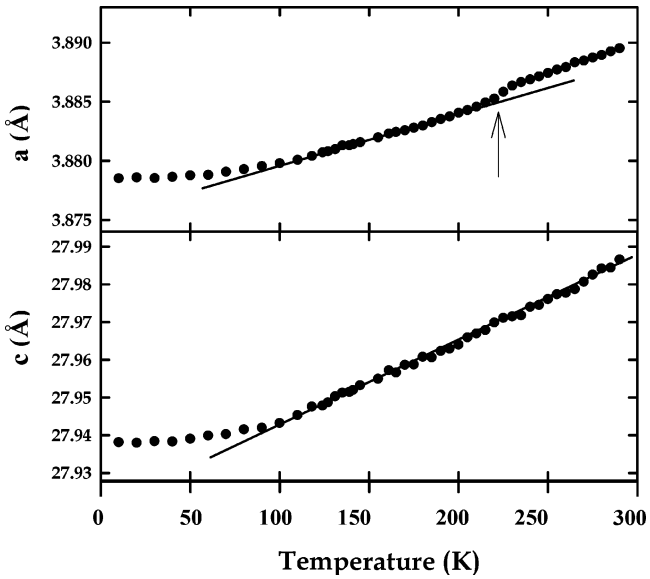

Figure 9. Evolution of the lattice constants as a function of the temperature.

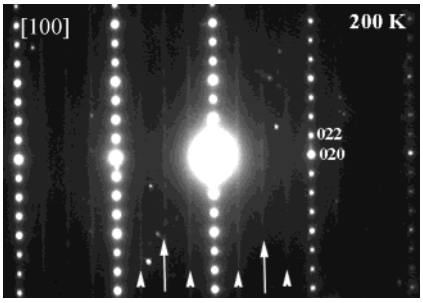

Figure 10. [100] ED pattern of $Sr_4Fe_2O_6CO_3$ registered at 200 K.

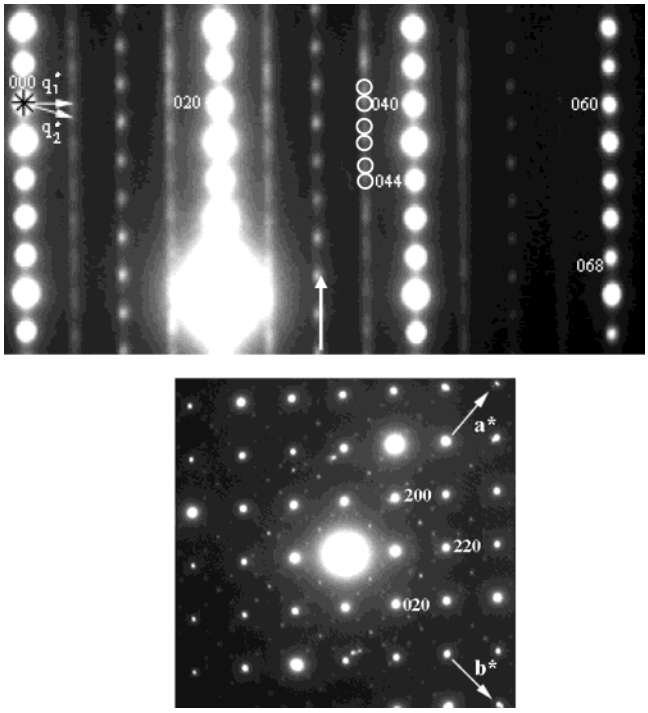

Figure 11. (a) [100] and (b) [001] ED pattern of $Sr_4Fe_2O_6CO_3$ registered at 90 K.

(5) Electron Microscopy Study at Low Temperature. The reciprocal space remains unchanged down to about 220 K. Below this temperature, one observes a deviation of the γ angle pointing to a monoclinic distortion; a second system of weak reflections appears, involving a doubling of the cell parameters $a_{LT} \approx b_{LT} \approx 2a \approx 2a_T\sqrt{2}$. The extra reflection first appears as weak diffuse streaky lines, but their intensity increases as T decreases (see white triangles in Figure 10).

Between 130 and 115 K, diffuse streaky lines of the *Aba*2 subcell (white arrows) are replaced by nodes in positions ($^1/_2$,0,l) and (0,$^1/_2$,l) with l odd. This phenomenon suggests that the structural disorder associated with the carbonate arrangement along $\vec{c}$ decreases, as shown in Figure 11a recorded at 92 K.

At 92 K, the doubling of the cell parameters is perfectly visible on the [001] ED pattern (Figure 11b) but the reconstruction of the reciprocal space shows that the actual structure is more complex since systems of nodes appear in the diffuse streaky lines as shown in the [100] ED pattern (see white circle in Figure 11a). Most of the ED patterns can be interpreted on the basis of the coexistence of two different modulated structures, with $a_{LT} \approx b_{LT} \approx 2a_T\sqrt{2}$, $c_{LT} \approx c = 28$ Å, $\gamma \approx 90° + \epsilon$ and with vector $\vec{q}_1 = {}^1/_2\vec{b}^*$ and $\vec{q}_2 = {}^1/_2\vec{b}^* + {}^2/_3\vec{c}^*$. These structural transitions are reversible.

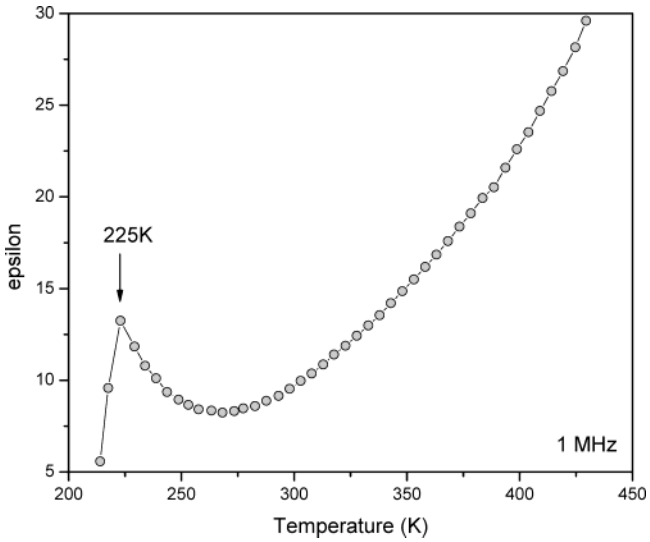

Figure 12. Evolution of the relative dielectric constant ϵ_r as a function of the temperature.

The electron diffraction study versus T shows a structural transition occurring at 220 K, which is associated with a monoclinic distortion and with the first signature of the appearance of a superstructure. The latter, not detectable by XRD and NPD classical diffraction techniques, coincides with the evolution of the Mz (Figure 8), Mössbauer results, and magnetotransport measurements (see next section). The second phenomenon detected between 130 and 115 K could likely mainly originate from a progressive rearrangement of the carbonate groups along $\vec{c}$, if one refers to the RT observations (Figure 4). An ED characterization down to 10 K would be necessary for determining further evolution of the ordering.

(6) Physical Characterizations. $Sr_4Fe_2O_6CO_3$ is an insulator. The bar, which has been tested, exhibits, from 5 to 400 K, an electrical resistivity superior to the limits of detection of the PPMS (5×10^6 Ω). The relative dielectric constant was measured from room temperature down to 210 K, which is the lowest possible temperature allowed by our equipment (see Figure 12). One can see a transition occurring at about 220 K which confirms the Mössbauer result for which the electronic environment of iron is disturbed at 220 K (see section Mössbauer). Further study of transport properties on single crystals would be of great interest to clarify this point.

Magnetization curves were recorded as a function of temperature in different applied magnetic fields (after zero-field cooling in all cases). In a range of intermediate fields (approximately between 0.25 and 6 T), a clear anomaly is detected around 220 K, as shown in Figure 13 in the case of 5 T. This transition is quite sharp (less than 10 K), and there is no significant difference between the curves registered upon warming or cooling. Note that the large upturn in susceptibility at low temperature is most likely related to a small amount of impurities, giving rise to a Curie−Weiss contribution. In a previous study of this compound,[7] the susceptibility was measured in a field of 9 T and no transition was

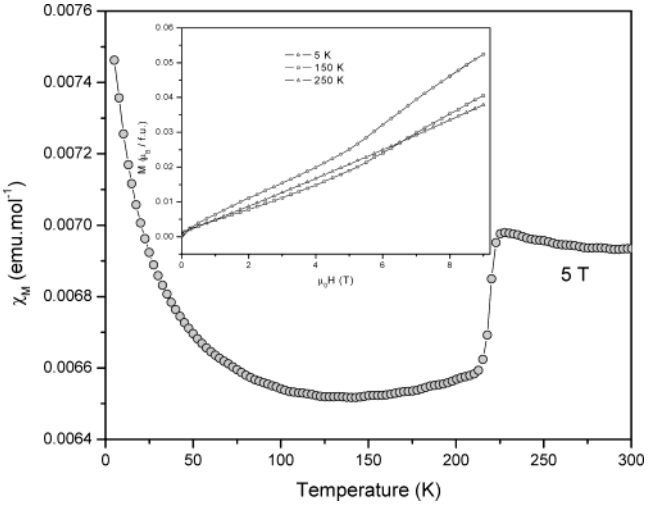

Figure 13. Evolution of the magnetic susceptibility as a function of the temperature. Inset: evolution of the magnetization as a function of the field, registered for different temperatures which are noted on the graph.

visible at 220 K. Our study confirms that this transition cannot be detected under too small or too large fields. The $M(H)$ curves displayed in the inset of Figure 13 shed light on this issue. We just considered here three characteristic temperatures: 5 K (very low T regime), 150 K (low-T side of the transition), and 250 K (high-T side of the transition). It is clear that the shape of the curves at 5 and 150 K are very different from the one at 250 K, revealing a significant change in the nature of the antiferromagnetic state. The latter curve is almost linear over the whole field range, while the other exhibits a rounding in the low field regime and an increase in slope above about 5 T. Since one deals with a ceramic sample, these last features might be related to a combination of canting and spin-flop phenomena (connected to field orientations perpendicular and parallel to the anisotropy axis, respectively). When recording $M(T)$ curves, it turns out that a clear signature of the transition (with an upturn step as in Figure 13) can only be observed in the intermediate field range when the $M(H)$ at 250 K is larger than that at 150 K.

To go further in the characterization of the transition at 220 K, with its apparent field dependence, heat capacity measurements were performed in zero field and in an applied field of 5 T. Figure 14 shows that, in both cases, a prominent peak develops around 220 K. This confirms that there is a bulk thermodynamic transition at this temperature, and it demonstrates that this transition also exists under zero field. Actually, in magnetization measurements, application of large enough fields is only required to *reveal* the transition. Spin-reorientation phenomena often produce sharp peaks in $C(T)$ as in Figure 14. In our case, note that the significant structural distortion associated with the spin reorientation must also take part in the specific heat anomaly. The inset of Figure 14 shows C/T versus T around the transition. This enlargement of the transition shows the absence of noticeable field dependence. Integration of this peak using a phenomenological linear background (line in the inset of Figure 14) leads to an entropy change at the transition that is close to 3 J K^{-1} mol^{-1}.

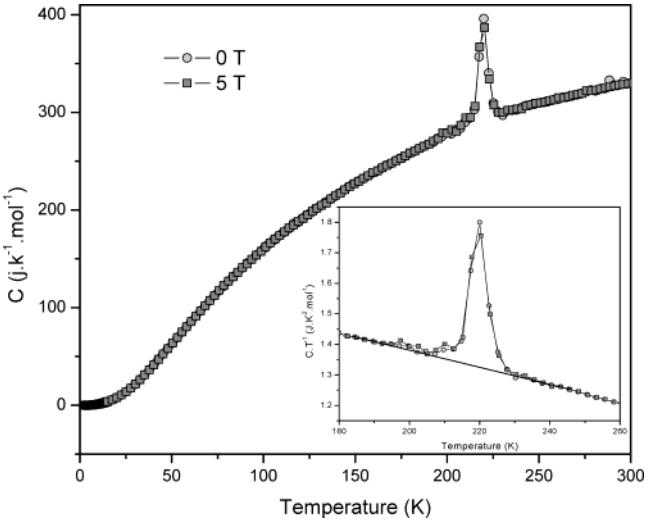

Figure 14. Evolution of the specific heat as a function of the temperature.

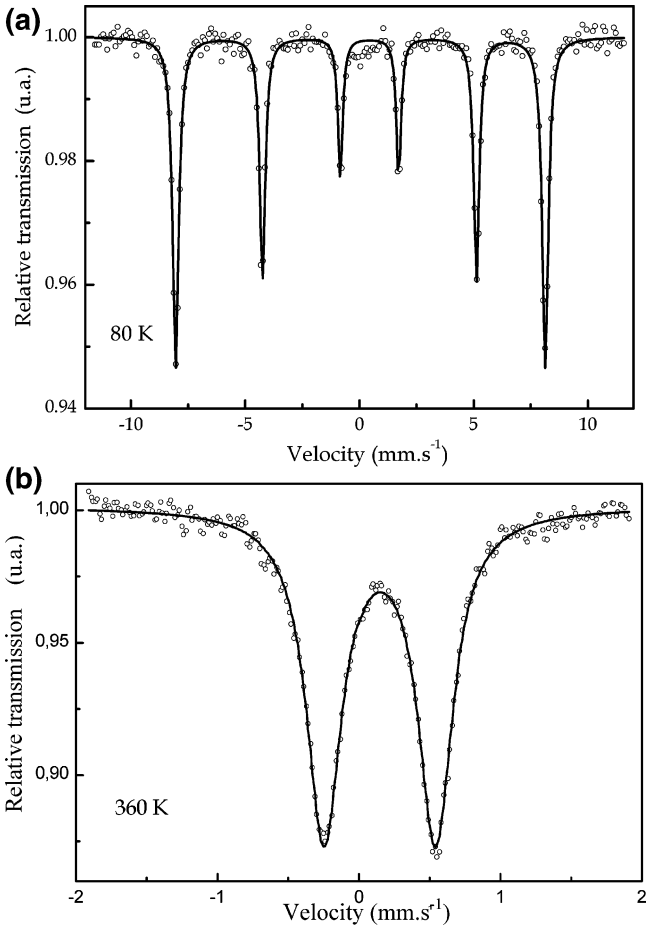

Figure 15. Mössbauer spectrum recorded at 80 K (a) and 360 K (b).

(7) Mössbauer Spectroscopy and Electric Field Gradient (EFG) Calculations. ^{57}Fe Mössbauer spectra were registered between 80 and 500 K.

The low-temperature spectra (80 K $\leq T \leq$ 340 K) (Figure 15a) were analyzed with one magnetic iron site which becomes paramagnetic at about 360 K, in agreement with ref 7. The isomer shift (IS) and hyperfine field (H_{hyp}) values (0.4 mm/s and 50.2 T at 80 K, respectively) are characteristic of high-spin Fe^{3+} and decrease when the temperature increases (Table 3). However, one

Table 3. Isomer Shift (IS), 2ϵ, Hyperfine Field (H_{hyp}), and |QS| Values versus Temperature

T (K)	IS/Fe (mm s^{-1}) ±0.005	2ϵ (mm s^{-1}) ±0.01	H_f (T) ±0.1 T	|QS| (mm s^{-1}) ±0.01
80	0.397	−0.39	50.23	
90	*0.395*	*−0.38*	*49.83*	
100	0.392	−0.39	49.42	
110	*0.391*	*−0.39*	*48.93*	
120	0.389	−0.39	48.28	
130	*0.385*	*−0.39*	*47.81*	
140	0.381	−0.39	47.32	
150	*0.379*	*−0.39*	*46.80*	
160	0.377	−0.39	46.20	
170	*0.369*	*−0.39*	*45.59*	
175	0.366	−0.39	45.29	
185	*0.363*	*−0.39*	*44.55*	
200	0.359	−0.39	43.44	
210	*0.355*	*−0.39*	*42.71*	
220	0.347	−0.39	41.85	
225	*0.348*	*−0.39*	*40.89*	
230	0.347	−0.39	40.89	
235	*0.347*	*−0.39*	*40.14*	
240	0.343	−0.39	39.96	
245	*0.332*	*−0.39*	*38.91*	
260	0.327	−0.39	37.55	
275	*0.318*	*−0.39*	*36.06*	
300	0.310	−0.39	30.70	
320	*0.296*	*−0.37*	*27.1*	
340	0.284	−0.38	22.0	
360	*0.270*			*0.77*
435	0.230			0.76
500	*0.180*			*0.75*

observes that the IS value is constant in the range 215−235 K (Figure 16) where the spectra were registered every 5 K. Despite its small effect, this event could be correlated to the transitions observed in the previous physical characterizations: relative dielectric constant ϵ_r, heat capacity, and magnetic susceptibility, in the same temperature domain (see previous sections). This accident on the IS(T) curve probably reveals a change in the s electron density of states at the iron nucleus. It could explain the modifications observed on the thermal variation of the relative dielectric constant $\epsilon_r(T)$ because, in the transition range, the modifications of the electronic shells around the iron nucleus lead very likely to a perturbation of the local electric field and of the mean polarizability $\bar{\alpha}$ of every dipole induced by the applied electric field. On the other hand, no change in the anisotropic part of the Mössbauer electric hyperfine interaction is observed; the quadruplole shift is indeed practically constant in the whole magnetic domain (−0.39 mm/s).

Contrary to IS, the thermal H_{hyp} evolution is continuous (Figure 17) and has been fitted using a Brillouin curve (solid line) with $H_{hyp}(0\ K) = 51.2(1)$ T, $T_N = 359(1)$ K, and $S = 2.5(1)$.

Above 340 K, in the paramagnetic domain, the spectra are well-fitted with one Lorentzian symmetric doublet (Figure 15b), its experimental line width being rather large ($\Gamma \approx 0.32$ mm/s). The IS value decreases from 0.27 mm/s at 360 K to 0.18 mm/s at 500 K (Table 3); this thermal variation is typical for a high-spin Fe^{3+} ion (Figure 16). The absolute value |QS| of the quadrupole splitting decreases from 0.77 mm/s at 360 K to 0.75 mm/s at 500 K (Table 3).

As the line width of the fitted doublet is approximately twice that of a standard one ($\Gamma \approx 0.15$ mm/s), it is probably due to a random distribution of QS values

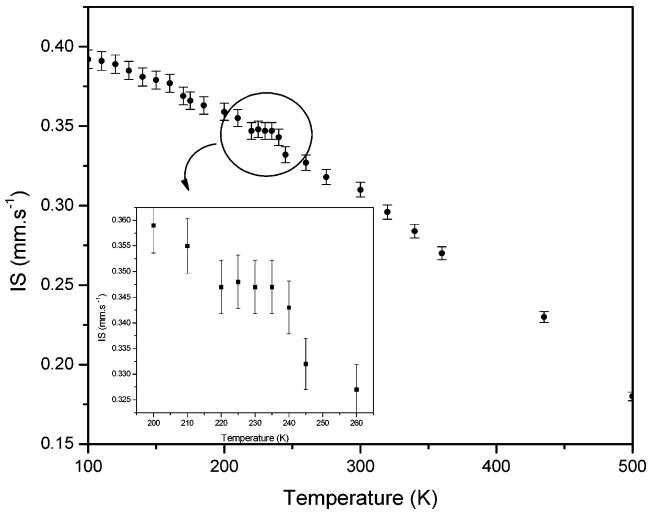

Figure 16. Evolution of the isomer shift as a function of the temperature.

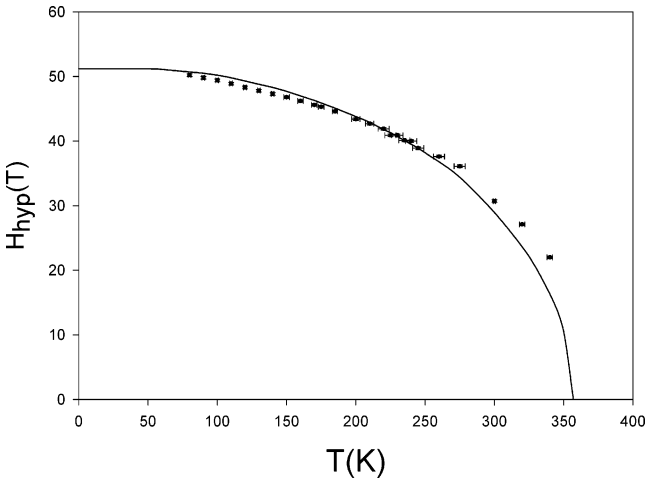

Figure 17. Thermal evolution of the experimental hyperfine field (dots) and the fitted Brillouin curve (solid line).

with a dispersion roughly estimated at 0.08 mm/s, on each side of the central fitted QS value.

It is known that, for an Fe^{3+} ion, the quadrupole splitting mainly results from the asymmetric part of the hyperfine electric interaction between the iron nucleus and its surrounding neighbors. Thus, the role on the Mössbauer spectra of the different carbonate configurations, in $Sr_4Fe_2O_6CO_3$, can be tested by doing EFG lattice calculations and by comparing the resulting calculated QS values to the experimental one. This would allow a better understanding of the origin of the large Γ values of the Lorentzian Mössbauer lines fit.

Thus, EFG calculations were performed for Fe^{3+} in several oxygen environments due to either the "coat hanger" (CH) configuration or the "flag" (F) one. The lattice [$\mathbf{V}_{ij}$] EFG tensor at the monopolar approximation of the potential development of a crystal field model was calculated for each iron surrounding, using a neutral "cluster" including only ions in the range $d_{Fe-ligand} \leq 7.8$ Å (number of considered ions = 122−137), with the atomic positions given by the neutron diffraction study at 500 K. The upper size has been retained after several convergence tests for the $\mathbf{V}_{ij}$ components, using cluster sizes varying between 5 and 8.5 Å. At this level, the maximum error resulting in QS values, due to the

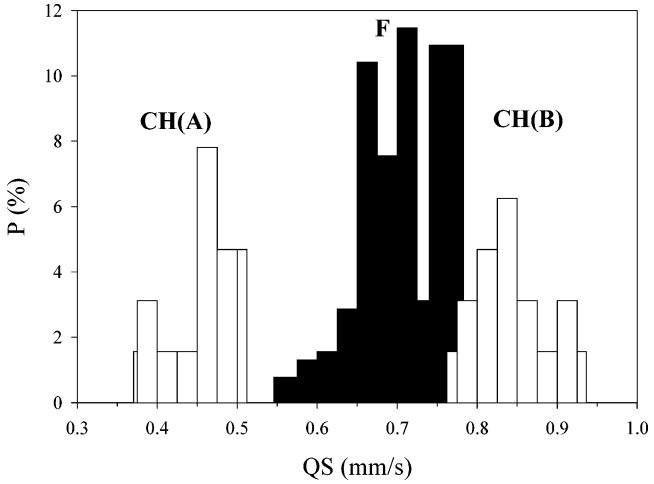

Figure 18. Calculated distributions of the Mössbauer quadrupole splitting QS of Fe^{3+} for "coat hanger" A (CH(A)) and B (CH(B)) and for "flag" (F). The discrete QS distributions have been gathered into class distributions with 0.025 mm/s of line width.

cluster size choice, is about 0.025 mm/s, and often much smaller.

The quadrupole splitting of the paramagnetic Mössbauer site can then be calculated using $QS = e(Q/2)(1 - \gamma_\infty)V_{ZZ}(1 + \eta^2/3)^{1/2}$ where $Q \approx 0.2$ barn[20] is the nuclear quadrupole moment of iron in its excited ($I = {}^3/_2$) state; $(1 - \gamma_\infty)$ is the antishielding Sternheimer factor[21] for Fe^{3+}; V_{ZZ} is the principal component of the $[\mathbf{V}_{ij}]$ lattice tensor and $\eta = (V_{XX} - V_{YY})/V_{ZZ}$ is the asymmetry parameter ($0 \le \eta \le 1$).

CH Configurations. Two cases must be analyzed depending on the number of oxygens surrounding the resonant Fe^{3+}: 5+1 (noted A in Figure 5b) if the metal is linked to the carbonate group or 5 (noted B in Figure 5b) if it is not.

(a) For Fe^{3+}(A), the first oxygen neighbors belonging to a CH carbonate are the apical O(3) at 2.623 Å and the two O(4) at 4.674 Å, with O(4)−O(4) parallel to $\vec{a}$ or $\vec{b}$.

(b) For Fe^{3+} (B), the first oxygen neighbors belonging to a CH carbonate are the two O(4) at 3.679 Å.

In an FeO_2 layer, each iron atom in the CH configuration can randomly adopt either the A or the B configuration, with equal probabilities. Along $\vec{c}$, each Fe^{3+}(A) is necessarily associated with an Fe^{3+}(B) distant of about 8 Å. The only constraint to be respected is the 90° rotation of neighboring carbonates. It results that one Fe^{3+}(A) or Fe^{3+}(B) ion has four first Fe^{3+}(A) or Fe^{3+}-(B) neighbors and can introduce 2×2^4 different carbonate environments which have been investigated.

The EFG calculations show that, in each case, the asymmetry parameter η is different from zero and the QS values are positive and lie in the following ranges: $0.371 \le QS_A \le 0.573$ mm/s, with $0.01 \le \eta_A \le 0.30$ and $0.763 \le QS_B \le 0.932$ mm/s, with $0.02 \le \eta_B \le 0.16$ (Figure 18).

The asymmetry parameter dispersions being large and the principal axes of the $[\mathbf{V}_{ij}]$ tensors being different from one situation to the other, two mean tensors $[\overline{\mathbf{V}_{ij}}]_{CHA}$ and $[\overline{\mathbf{V}_{ij}}]_{CHB}$ must be calculated, for which equal probabilities were taken for each of the different carbonate environments. The final diagonalizations lead to $\overline{QS_A} = 0.456$ mm/s ($\overline{\eta_A} = 0.08$) and $\overline{QS_B} = 0.847$ mm/s ($\overline{\eta_B} = 0.15$) with standard error deviations of 0.036 and 0.058 mm/s, respectively. As one Fe^{3+}(A) is necessarily associated with one Fe^{3+}(B) along $\vec{c}$, the total distribution of QS, which admits $\overline{QS_{CH}} = 0.652$ mm/s, was finally considered, but with a very large standard error deviation of 0.223 mm/s around this central value. This standard error is too high to agree with the experimental one (0.08 mm/s). So the real distribution of the carbonates cannot be only of CH-type, in agreement with the structural and IR results.

Calculations of QS, considering the effects of CO_3 groups at the level of second next iron neighbors, have been tested for several configurations and showed that they can be neglected.

F Configurations. There is only one type of iron site to examine (Figure 5a). The two O(5) atoms of each carbonate link the two pseudo octahedral Fe^{3+} centers stacked along $\vec{b}$. The first O(5) lies at 2.98 Å from the central considered Fe^{3+} atom and the second one at 5.16 Å. The oxygen O(6) is at the apex of the CO_3 triangle, at 4.257 Å from Fe^{3+}. The C−O(6) directions are randomly parallel (or antiparallel) either to $\vec{a}$ or to $\vec{b}$ (respectively noted →, ←, ↑, or ↓). Along one direction, 90° rotation is allowed (for example, ...→↑→↓←...), but steric constraints make some carbonate orientations forbidden: along one direction, two next neighbors can have the same CO(6) orientation (→ → or ← ← or ↑↑ or ↓↓) but cannot adopt the antiparallel orientations as → ←, while orientation ← → is allowed.

For one central Fe^{3+} species (for instance, of → type), with four next iron neighbors (at 3.9 Å) we can theoretically predict $2^4 \times 2^4 = 256$ different carbonate configurations; only 192 of them respect the above steric constraints. We have done EFG calculations for each of these 192 "F" configurations. As for CH configurations, the carbonate disorder on the 4 s iron neighbors of the central Fe^{3+} can be neglected.

The QS_F and η_F values, obtained after diagonalization of the 192 $[\mathbf{V}_{ij}]$ lattice tensors lie in the range $0.558 \le QS_F \le 0.773$ mm/s (Figure 18), with $0 \le \eta_F \le 0.44$. A weighted mean tensor $[\overline{\mathbf{V}_{ij}}]_F$ has been calculated, taking equal probabilities for each of the 192 configurations leads to $\overline{QS_F} = 0.705$ mm/s with $\overline{\eta_F} = 0.12$. The distribution of QS_F values has a standard error deviation of 0.049 mm/s, too small to explain the experimental one. So the real distribution cannot be of F-type only.

Finally, as suggested by the structural study, a mixing of 50% CH and 50% F configurations was considered and using the tensors associated with the previous CH and F distributions, a mean $[\overline{\mathbf{V}_{il}}]$ tensor was calculated. This leads to $\overline{QS} = 0.675$ mm/s and $\bar{\eta} = 0.12$, with a global standard error deviation of 0.15 mm/s for QS. The central $\overline{QS}$ value lies in the experimental range but the calculated dispersion is still a little greater than the experimental one.

The origin of the difference between the last $\overline{QS}$ value and the experimental QS one could result from several factors, among them the fact that, in the last

(20) Gütlich, P.; Link, R.; Trautwein, A. *Inorganic Chemistry Concepts, Vol. 3, Mössbauer Spectroscopy and Transition Metal Chemistry*; Springer-Verlag: Berlin 1978.

(21) Sternheimer, R. M. *Phys. Rev.* **1963**, *130*, 1423.

mixed case, it was supposed that the first in-plane iron neighbors of a CH or F site have the same configuration as the central iron. This hypothesis agrees with HREM observations and allow the above CH and F results to be used but some deviations to this perfect ordering cannot be ruled out. In an other way, the CHA, CHB, and F configurations, which have been considered with equal weighting factors in the calculations of $[\overline{\mathbf{V}_{ij}}]_{CHA}$, $[\overline{\mathbf{V}_{ij}}]_{CHB}$, and $[\overline{\mathbf{V}_{ij}}]_{F}$ could occur with different unknown probabilities in the distribution.

Nevertheless, despite all these approximations, the EFG allows one to understand the broad experimental line width value of the Mössbauer paramagnetic doublet and reinforce the mixing of F and CH carbonates, in agreement with the structural and IR results.

Conclusion

The structural study of the oxycarbonate $Sr_4Fe_2O_6CO_3$ showed that it crystallizes in an orthorhombic cell and exhibits disorder phenomena between successive layers of carbonates, which are nondetectable by neutrons or X-ray diffraction. At 220 K, a monoclinic distortion occurs, which is accompanied by an accident in the thermal evolution of the parameter *a*. This distortion is also accompanied by a spin reorientation ($\approx$7°) and a modification in the electronic environment of iron. It is difficult to say if one of these phenomena is at the origin of the others. Further study on single crystal would be of interest to clarify all these points. Mössbauer spectroscopy confirms the high-spin state of Fe^{3+} ions and EFG calculations allow one to understand the unusual broadening of the Mössbauer lines.

Acknowledgment. The authors are extremely grateful to Pr. Marco Daturi (Laboratoire de catalyse et spectrochimie, Ensicaen, France) for collection of IR data and helpful discussions, Dr. Mikael Pollet (Laboratoire CRISMAT) for dielectric measurements, and Dr. Jean Marc Grenèche (Laboratoire de Physique de l'Etat Condensé, UMR CNRS 6087, Université du Maine, Le Mans, France) for high-temperature Mössbauer spectra.

CM0401241